# BODY-WAVE ARRIVALS FROM SEISMIC NOISE

Jian Zhang[1], Peter Gerstoft[1], Steven R. Taylor[2]

University of California, San Diego[1] and Rocky Mountain Geophysics, LLC[2]

Sponsored by Air Force Research Laboratory

Contract No. FA8718-07-C-0005

## ABSTRACT

Array analysis of body-wave seismic noise has the potential to be very useful in improving body-wave tomography of Earth structure, just as noise cross-correlation methods have recently proven successful in surface-wave tomography. Beamforming of seismic noise recorded in southern California reveals *P*-wave arrivals from distant storms in open oceans. In this case, the noise can be processed using cross-correlation among different station pairs and optimal *P*-wave relative arrival times can be estimated using the same approach traditionally used to analyze earthquake arrival times.

Using three storms in the Gulf of Mexico, the Western Pacific (near Japan), and the South Pacific (near Fiji) respectively, we demonstrate that travel-time anomalies can be obtained from *P* waves generated by a distant storm, and that they are similar to those obtained from using an earthquake close to the storm. Our results suggest using oceanic storms as additional seismic sources for resolving *P*-wave travel-time anomalies.

The accurate identification of *P*-wave microseism source areas is also useful to monitor ocean wave-wave interactions due to tropical cyclones. Nonlinear wave-wave interactions generate double-frequency (DF) microseisms, which include both surface waves (mainly Rayleigh-type) and compressional (*P*) waves. Although it is unclear whether DF surface waves generated in deep oceans are observed on land, we show that beamforming of land-based seismic array data allows detection of DF *P* waves generated by ocean waves from Super Typhoon Ioke in both pelagic and coastal regions.

Two distinct spectral bands associated with different *P*-wave source locations are observed. The short-period DF band (0.16–0.35 Hz) is dominated by *P* waves generated in the deep ocean by local wind seas under the storm. In contrast, *P* waves in the long-period DF band (0.1–0.15 Hz) are weaker and generated closer to the coast of Japan from swell interactions.

## OBJECTIVES

Our objective is to seek turning storm-generated body-wave seismic noise into relative arrival time estimates, and thus improving traditional body-wave tomography by filling the azimuthal gaps of seismic sources. We also tend to determine if deep-ocean source areas of microseismic *P* waves can be definitively identified using frequency-domain beamforming of land-based seismic array data, and to distinguish distinct SPDF and LPDF *P*-wave microseism source areas through spectral analysis of the beamformer outputs.

## RESEARCH ACCOMPLISHED

### Resolving *P*-Wave Travel-Time Anomalies using Seismic Array Observations of Oceanic Storms

This section is based on Zhang et al. (2010a). Since the pioneering studies by K. Aki and colleagues in the mid 1970s (Aki et al., 1976, 1977; Husebye et al., 1976), teleseismic *P*-wave travel-time anomalies derived from using earthquakes have been providing the data for inferring three-dimensional (3-D) velocity heterogeneities beneath seismic networks or arrays, i.e., regional/local body-wave tomography. However, inhomogeneous data coverage, particularly the absence of both earthquakes and seismic instruments in many open oceans, has long been a challenge for seismic imaging. For teleseismic body-wave tomography, this may result in poor coverage of certain directions. Studies of phase delay times across southern California, for instance, have been hampered by azimuthal gaps to the south and northeast (e.g., Humphreys and Clayton, 1990; Polet, 2007). Thus, additional seismic sources, if available, could help fill azimuthal gaps in the data. An alternative to earthquakes (and/or controlled sources) is storms. Hiding in microseisms there are non-pulse-like yet coherent *P* waves that are generated by oceanic storms, which can be revealed by seismic array observations. *P* waves from storms have been reported as early as in the late 1960s (Toksoz and Lacoss, 1968; Lacoss et al., 1969; Haubrich and McCamy, 1969), but then received little attention until Hurricane Katrina "hit" California and Gerstoft et al. (2006a) were able to characterize and back-project the hurricane-generated *P* waves with beamforming of seismic noise recorded at the Southern California Seismic Network (SCSN). Modern array techniques now have allowed the accumulation of more observations of *P* waves that can be associated with sea states and even specific storms (Gerstoft et al., 2008; Koper and de Foy, 2008; Landes et al., 2008; Koper et al., 2009; Zhang et al., 2009).

Noise cross-correlation (NCC) of coherent *P* waves such as those observed in Gerstoft et al. (2006a and 2008) at the SCSN can therefore be used to measure the time lag of *P* arrivals between a pair of stations, and thus lead to estimates of relative *P*-wave arrival times across an array from distant noise sources. These relative arrival times, if accurate enough, contain information about seismic velocity anomalies under the array. This suggests that it may be possible to supplement earthquake data with *P*-wave microseisms from areas of active storms, for performing regional body-wave tomography of crust and upper-mantle structure. It should be noted that NCC processing has recently become popular in extracting Green's functions from seismic noise (Shapiro and Campillo, 2004; Snieder, 2004; Wapenaar, 2004; Sabra et al., 2005a), which has made possible the use of ambient noise for surface-wave tomography (Shapiro et al., 2005; Sabra et al., 2005b; Yao et al., 2006, 2008; Kang and Shin, 2006; Yang et al., 2007, 2008; Moschetti et al., 2007; Lin et al., 2007, 2008; Liang and Langston, 2008; Zheng et al., 2008).

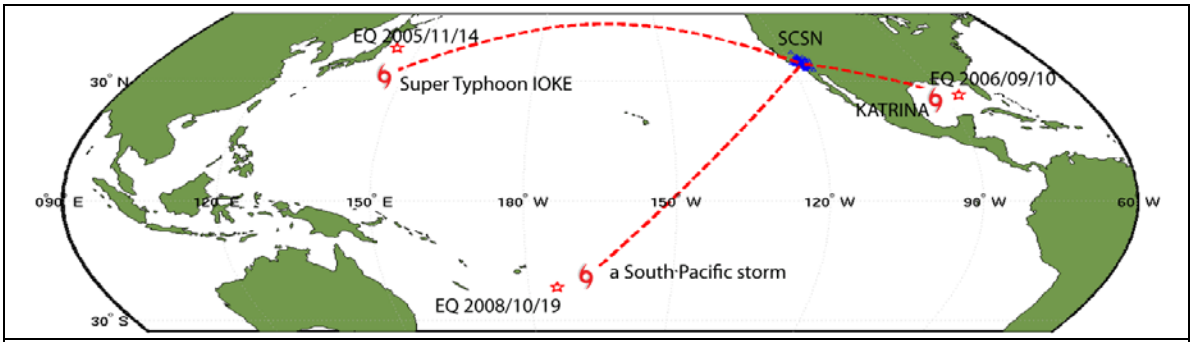


**Figure 1. Locations of the SCSN, Hurricane Katrina (schematic), an Mw 5.9 earthquake on September 10, 2006, Super Typhoon Ioke (schematic), an Mw 7.0 earthquake on November 14, 2005, a South Pacific storm (schematic), and an Mw 6.9 earthquake on October 19, 2008. The dashed lines indicate the great circle paths of the *P* waves from the storms to the SCSN.**

We demonstrate in this paper that the delay times measured from NCC processing of *P* waves from storms, which are "bias events" in terms of extracting Green's function for surface-wave tomography, can in fact provide travel-time anomaly information for teleseismic body-wave tomography. In particular, we identify and characterize the direct *P*-wave arrivals observed at the SCSN from three storms (see Figure 1) – Hurricane Katrina in the Gulf of Mexico, Super Typhoon Ioke in the Western Pacific (near Japan), and a storm in the South Pacific (near Fiji). We then validate the basic approach by following VanDecar and Crosson (1990) to obtain relative arrival times. For each storm we calculate the *P*-wave travel-time anomalies beneath southern California, and compare the result with that derived from using an earthquake close to the storm. It is noteworthy that these storms are at relatively great distances from the SCSN (~ 27–78$^o$), so that the *P*-wave arrivals can be approximated as plane waves, just as is commonly done when using earthquakes in teleseismic tomography.

Our analysis starts with array beamforming for identifying *P*-wave arrivals in seismic noise, as well as their sources. We use continuous vertical-component data (sampled at 1 s) recorded at the SCSN for the time window covering Hurricane Katrina's landing (August 28–29, 2005), and also for the whole year of 2006. Note that a 1-s sample rate allows faster beamforming yet is sufficient for identifying coherent microseisms. The data are truncated to no more than half of the daily standard deviations to mitigate contamination from occasional large-amplitude events (e.g., earthquakes). Beamforming is done within each 3-hour window for each 0.02-Hz bandwidth (details in Gerstoft et al., 2006a, 2008). By comparing the beamformed source regions with the ocean-wave hindcast data (Tolman, 2005), many *P*-wave events in the microseisms during 2006 are found to be due to specific storms. These storms, plus Katrina, serve as candidates for the NCC processing. For each storm we then compute the NCC time series (time lags up to 400 s, using data sampled at 0.05 s) among all station pairs and construct range-time plots to show propagating waves. Note that the ranges are the station separations projected along the storm direction, obtained from the beamformer output. We use a passband of 0.18–0.25 Hz for the NCC processing, in order to focus on the *P*-wave microseisms.

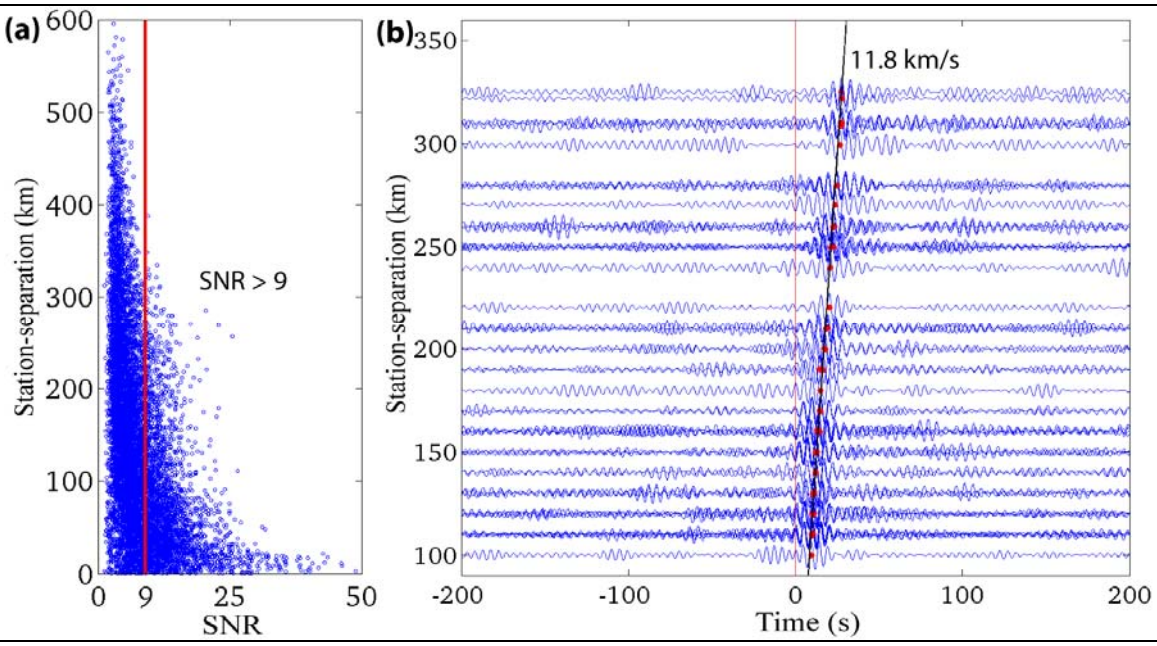


**Figure 2. Delay- time measurements from using Hurricane Katrina. (a) SNR vs. station-separation (projected along 100$^o$). The vertical line indicates a SNR of 9. (b) Range-time representation of the noise cross-correlation (NCC) time series for sample station pairs with SNR > 9. Dots in (b) mark the delay-time measurements (offsets of the NCC peaks) of *P* waves for each pair of stations. The thick line indicates an 11.8 km/s plane wave.**

A typical storm suitable for travel-time analysis should reach a sufficient signal-to-noise ratio (SNR) for its NCC peaks, so as to show up as an apparent propagating wave associated with its *P*-wave speed from beamforming. We define the SNR as the ratio of the peak in the *P*-arrival window (+/- 20 s of the plane-wave arrival as derived from beamforming) to the standard deviation for a "noise-only" window (300–400 s of an NCC time series). For example

in Fig. 2b, a propagating *P* wave from Katrina can be clearly seen in the range-time representation of the NCC time series of 400 station pairs (only a fraction is shown) with a SNR above 9, calculated for 1-day data (UTC 18:00 August 28 to UTC 18:00 August 29, 2005). Besides the SNR criterion, we apply a cutoff range over 100–400 km, given that there is an ambiguity between *P*-wave and coastal surface-wave arrivals at shorter ranges, and that times at longer ranges may not be well represented by the plane-wave assumption. In addition to Katrina, we have collected two more storms in 2006 (Fig. 1) for performing relative arrival-time measurements. For each of them, the *P*-wave delay time of each station pair is simply the offset of the maximum of the NCC function, e.g., see the dots in Fig. 2b. Instead of 1-s data for beamforming analysis, however, here we use the data sampled at 0.05 s for picking the peak times of the NCC functions, in order to obtain the delay-time estimates with a higher precision. Moreover, we select only delay-time measurements within +/- 2 s relative to the plane-wave arrival times approximated by the beamforming result. This criterion can remove large outliers, yet still covers the magnitude of typical regional travel-time anomalies.

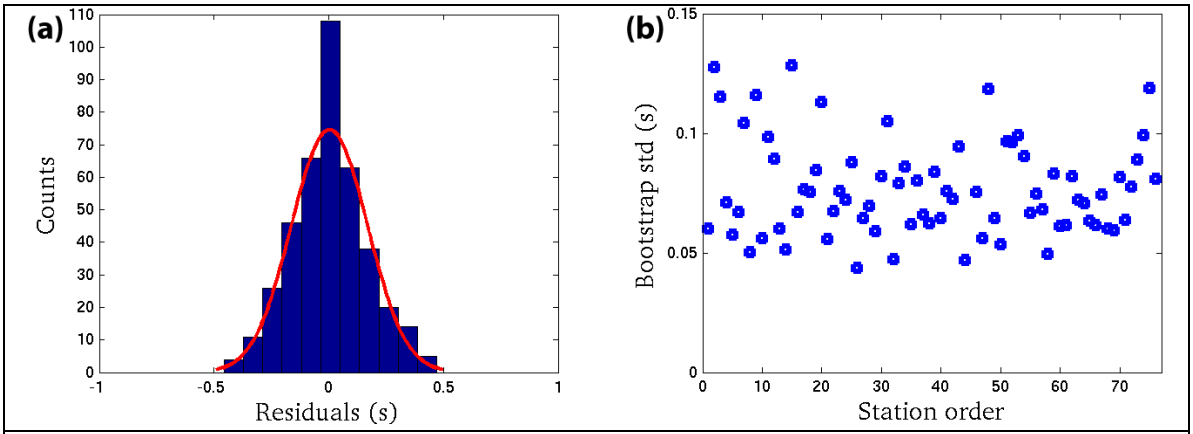


**Figure 3. Least-squares residuals and uncertainty estimation in differential times obtained from using Hurricane Katrina. (a) Histogram of equation residuals derived from the best-fitting solutions, showing a Gaussian-like distribution. The curve indicates a fitted normal distribution. (b) Bootstrap-resampling derived timing uncertainties of the *P*-wave relative arrival times for each station.**

Our approach of determining travel-time anomalies follows VanDecar and Crosson [1990]. We optimize relative arrival-time estimates through using least squares to solve an overdetermined system of delay-time equations, assuming that errors in the NCC derived delay times are primarily random in nature. For station pairs with a sufficient SNR, we generate equations given by $t_i - t_j = \Delta t_{ij}$. This system is expressed as $A \cdot t = \Delta t$. $A$ is a $M \times N$ sparse coefficient matrix, where $M$ is the number of equations and $N$ is the number of stations. The $i^{th}$ and $j^{th}$ columns of $A$ in a row associated with $\Delta t_{ij}$ are 1 and -1 respectively, while the other columns are zeros, and we add the constraint equation $\sum t_i = 0$ to force the arbitrary mean of the relative arrival times to be zero. Note that $N < M < (N-1) \cdot N/2 + 1$, as only the pairs with SNR above a certain criterion are used. A standard least-squares fit $t^{est} = A^{+} \cdot \Delta t$, where the pseudoinverse $A^{+} = (A^T \cdot A)^{-1} \cdot A^T$, can be found by applying singular value decomposition (SVD) and truncating small singular values. We repeat the procedure by removing outliers, i.e., the station pairs with a residual over 3 times the standard deviation of all residuals. Typically a stable solution is obtained after 4 iterations. For large systems in which SVD becomes computationally impractical, iterative methods such as the conjugate gradient algorithm LSQR of Paige and Saunders [1982] can be used to find the solution $t^{est}$.

We have found that the equation residuals $res_{ij} = \Delta t_{ij} - (t_i^{est} - t_j^{est})$ derived from the best-fitting solutions are nearly Gaussian-type distributed. An example is shown in Fig. 3a for the Katrina result. This suggests that the least-squares solutions can provide reasonable estimates of the relative arrival times. In addition, to evaluate the accuracy of the least-squares estimates of the relative *P* arrival times using seismic noise, we perform a statistical resampling analysis (i.e., the "bootstrap" method, Efron, 1982; Shearer, 1997; Waldhauser and Ellsworth, 2000) by replacing

the equation residuals with a randomly chosen set of residuals from the best fitting solutions. The process is then repeated 200 times, and the standard deviation of these bootstrap outputs provides an estimate of the timing uncertainty for each station. Fig. 3b shows, for an example of the Katrina, that a level of 0.1 s in timing errors can be reached, which should be sufficient for resolving typical *P*-wave travel-time anomalies on the order of 1 s.

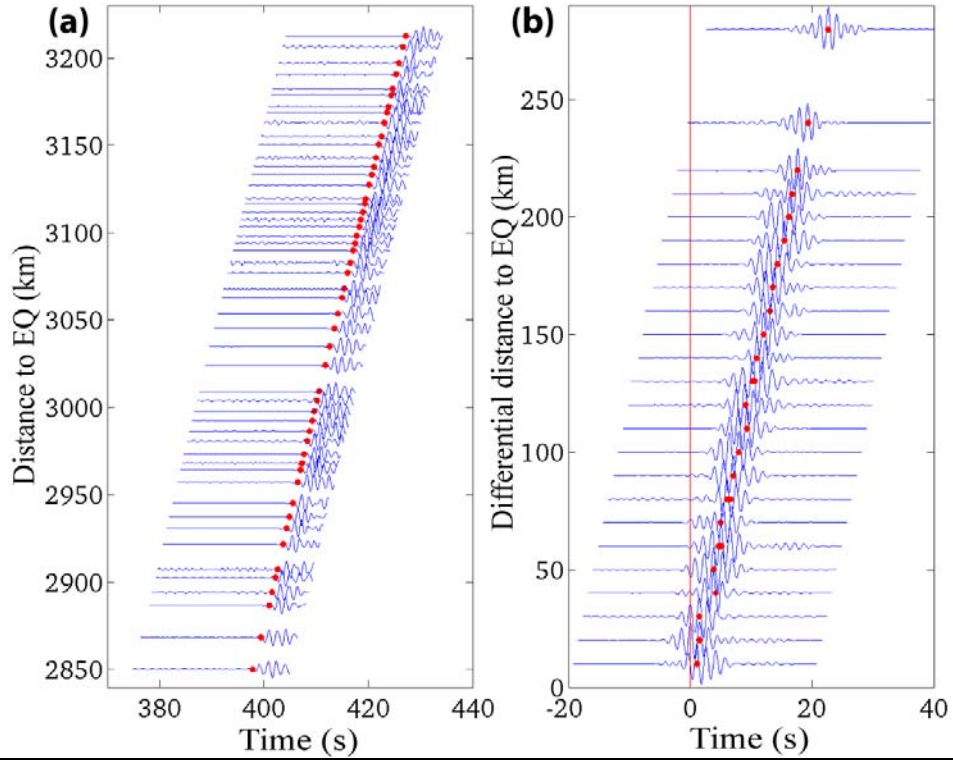


**Figure 4. Delay-time measurements from using EQ 2006/09/10. (a) Waveforms of the *P*-wave arrivals at the sample SCSN stations from EQ 2006/09/10. Dots mark the *ak135*-predicted travel times at each station. (b) Range-time representation of the earthquake waveform cross-correlation time series for sample station pairs. Dots mark the delay-time measurements (offsets of the cross-correlation peaks).**

To demonstrate the accuracy of the approach for using *P*-wave noise from the three storms, for each one we find an appropriate earthquake (Fig. 1) that is close to the storm and big enough to produce clear *P* pulses at the SCSN stations. We process the earthquake data in the same manner as described above. The principal difference to the NCC processing is that the cross-correlation using the earthquake signals takes advantage of the waveform similarity of the direct *P* arrivals in a short time-window, unlike using non-pulse-like noise, which requires coherence in a relatively long time-window. An example range-time plot of pulse-like *P*-wave arrivals and the waveform cross-correlation traces (only a fraction) is shown in Fig. 4 for an earthquake near Katrina (EQ 2006/09/10).

We then compare the results obtained from using storms and earthquakes respectively, for the relative *P*-wave arrival-time estimates, and accordingly for the *P*-wave travel-time anomalies as well. Anomalies are calculated as the zero-mean difference between the relative arrival-time estimates and the modeled relative arrival times. Upon choosing a reference arrival-time model, an earthquake can be regarded as a point source and thus the modeled arrival times can be calculated using the earthquake location and a standard Earth model, e.g., *ak135* (Kennett et al., 1995). When using a storm, the source point of its peak *P*-wave energy may be approximated by the location of the peak beam power. Thus the modeled arrival times can be calculated in the same way as is used for an earthquake. Alternatively the azimuth-slowness beam can provide a plane-wave reference model of the relative arrival times from a storm, without the need for a precise source location. We have noticed that the two methods result in very similar anomaly patterns.

The first comparison is shown in Fig. 5 for Hurricane Katrina (~ 27° away from the SCSN) and an Mw 5.9 earthquake that occurred in the Gulf of Mexico on September 10, 2006 (see Fig. 1 for the storm and earthquake locations). The relative *P* arrival times estimated by using Katrina noise and their residuals relative to a plane-wave arrival (with an apparent speed of 11.8 km/s and a back-azimuth of 100°) are shown in Figure 5a and c respectively. Similarly, the estimates using the earthquake and their residuals relative to the *ak135*-predicted arrival times are shown in Figure 5b and d respectively. It can be seen that the travel-time anomalies obtained from using Katrina-generated *P* waves are well correlated with those from an earthquake in the same source region. For example, the slow anomalies at the Mojave Desert side of the San Andreas Fault (SAF) and the Los Angeles basin (see Fig. 5f for the basic geological features) are observed both from Katrina (Figure 5c), and EQ 2006/09/10 (Figure 5d). To quantify this, the correlation coefficient between the two anomaly patterns is 0.62, with a significance level over 99%, calculated by using the noise vs. earthquake anomalies at 80 common stations (see also a scatter-plot in Figure 5e).

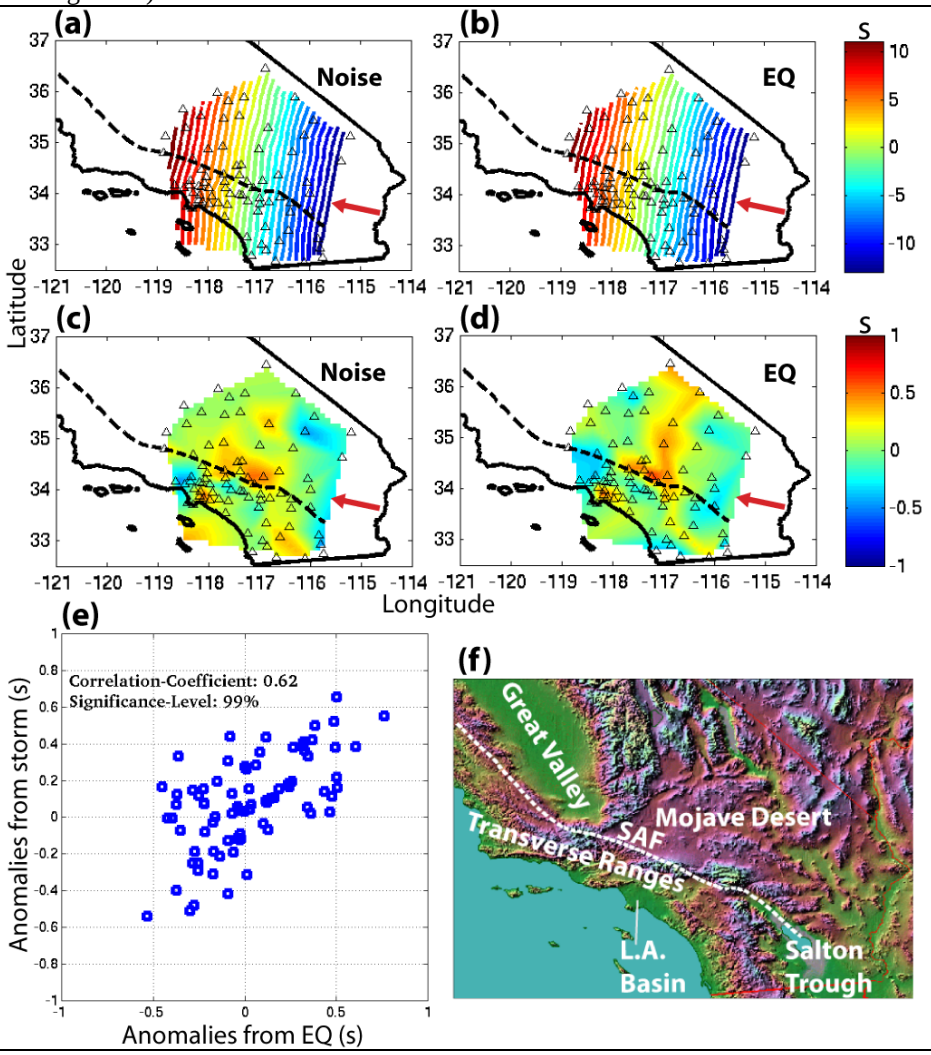


**Figure 5. Relative *P* arrival times in southern California as determined by using (a) Katrina, compared with those as determined by using (b) EQ 2006/09/10. Maps are also shown for *P* travel-time anomalies obtained from (c) subtracting a plane wave (100° in back-azimuth and 11.8 km/s in speed) from the NCC-derived arrival times in (a), compared with those obtained from (d) subtracting the *ak135*-predicted arrivals of EQ 2006/09/10 from the EQ-derived arrival times in (b). The used stations (triangles) and the San Andreas Fault (SAF) trace (dashed) are indicated in the maps. Arrows indicate the direction of the *P*-wave arrivals. (e) Scatter plot of EQ-determined anomalies vs. noise-determined anomalies at all common stations. (f) A topographic map showing the basic geological features of southern California.**

We find that this approach also works well for storms at longer distances. The second example is given in Fig. 6 by repeating the above procedure for Super Typhoon Ioke during September 5, 2006, which was ~ 75° away from the SCSN. Ioke appears in the beamformer output with a slowness of 0.051 s/km (19.6 km/s) and a back-azimuth of 300°. An Mw 7.0 earthquake near Japan on November 14, 2005 (Figure 1) is used to show a comparison of its *P*-wave relative arrival-time estimates with those obtained from using Ioke-generated *P* waves. Lastly we show in Fig. 7 the anomaly pattern from using a South Pacific storm (~ 78° away from the SCSN) during July 1, 2006, compared with that from an Mw 6.9 earthquake near Fiji on October 19, 2008, (Figure 1). This South Pacific storm appears in the beamformer output with a slowness of 0.05 s/km (20 km/s) and a back-azimuth of 228°. In Figures 6 and 7 respectively, once again a good correlation between the noise- and earthquake-derived anomaly patterns is directly visible in the map and quantified in the scatter plot. Typical agreement can be seen over regions such as the Great Valley, the Transverse Ranges, and the Salton Trough, further proving that *P*-wave travel-time anomalies can be resolved by using storms. Although beyond the scope of this work, one may also notice the large variation of the anomaly pattern obtained from events (either storms or earthquakes) with different directions and/or distances. Across the Salton Trough, for instance, Figure 6 shows fast anomalies whereas a slow pattern can be seen in Figure 7. Such differences can be used to image the heterogeneities at depth using tomographic inversion methods.

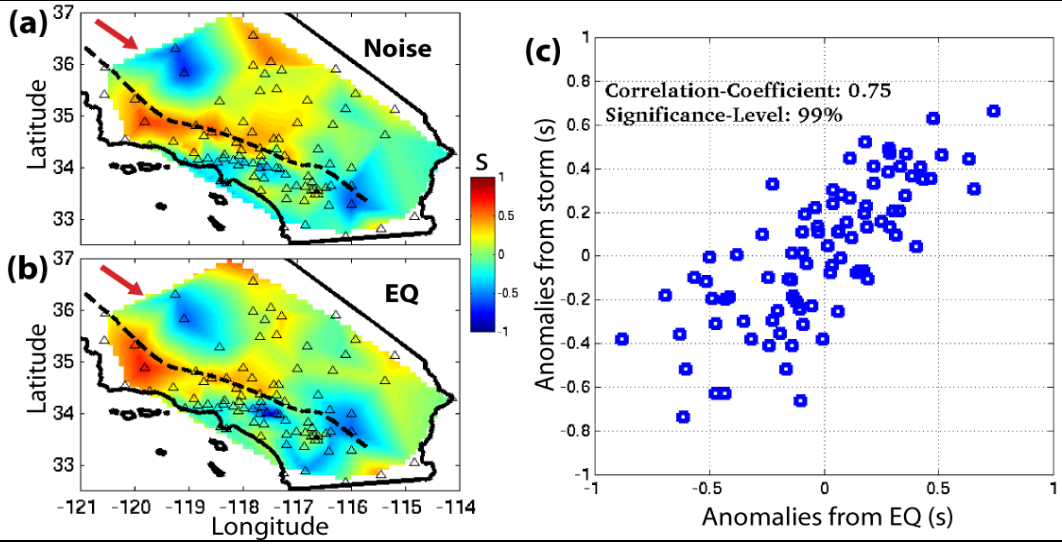


**Figure 6. Comparison of the result from using (a) Super Typhoon Ioke with that from using (b) EQ 2005/11/14, and thus their scatter plot (c), similar to Fig. 5c – e.**

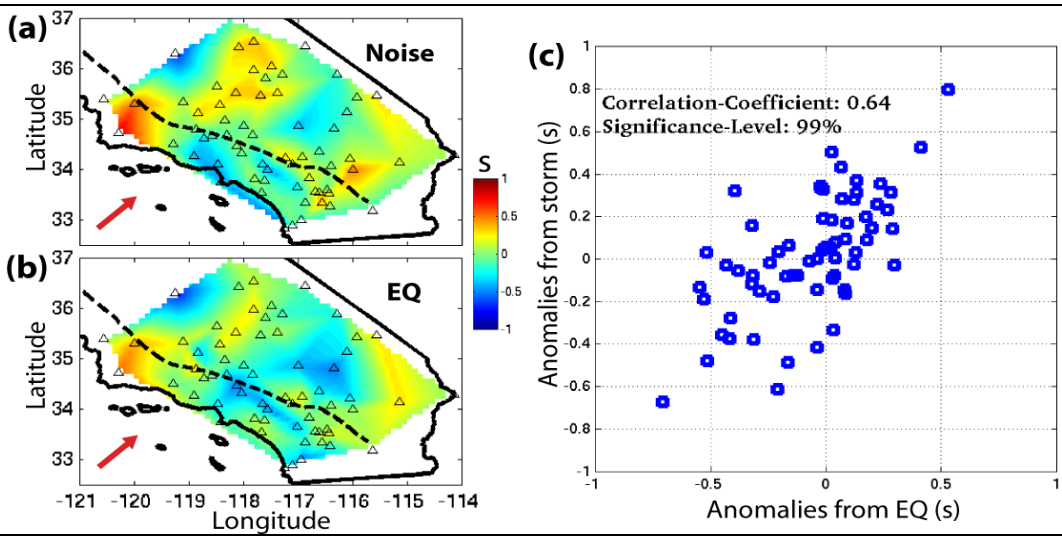


**Figure 7. Comparison of the result from using (a) a South Pacific storm with that from using (b) EQ 2008/10/19, and thus their scatter plot (c), similar to Fig. 5c – e.**

**Pelagic and Coastal Sources of *P*-Wave Microseisms: Generation under Tropical Cyclones**

This section is based on Zhang et al. (2010b). Strong coherent *P* waves generated under Super Typhoon Ioke (Figure 8a) are revealed and traced back to their origin locations via array beamforming of the microseisms recorded at the SCSN and the Hi-net respectively. First we focus on the SPDF band (about 0.16–0.35 Hz), as the power of *P*-wave beams peaks around 0.2 Hz. Tests show that *P*-wave energy is below the array noise floor at frequencies greater than 0.35 Hz. The trace of *P*-wave source locations, derived from using data at the SCSN, follows the path of Ioke (Figure 8b; typical beamformer output is shown in the insert). The source locations can also be identified using data from 79 southern stations of the Hi-net (Figure 8c), although the precision is relatively poor, in part due to the array geometry and the relatively short distance of Ioke from the array. Comparison of the *P*-wave source paths with the track of Ioke indicates that these *P* waves originated in the deep ocean near Ioke. This provides evidence that nonlinear wave-wave interactions in deep oceans generate *P*-wave microseisms that can be observed by land stations.

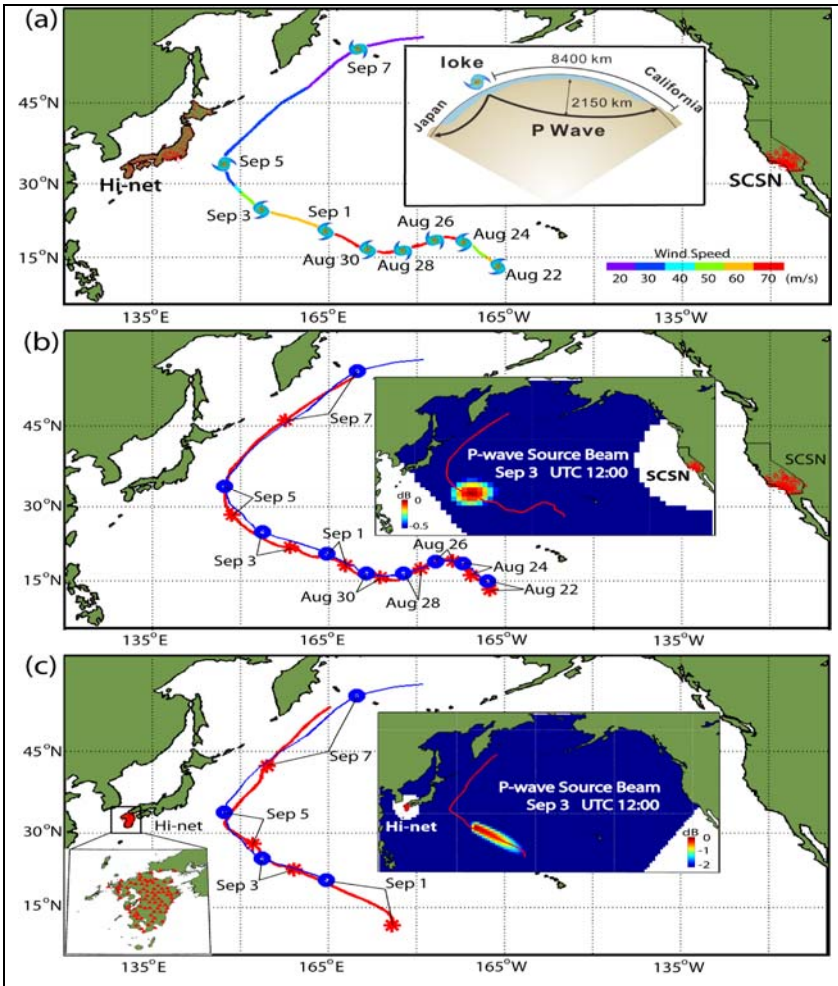


**Figure 8. Pelagic *P*-wave microseism sources tailing Super Typhoon Ioke. (a) Locations of the two arrays (SCSN and Hi-net, red), and the best-track of Super Typhoon Ioke (August 22 – September 7, from National Hurricane Center http://www.nhc.noaa.gov/) with wind speed indicated (color scale) and a schematic of *P*-wave ray paths from Ioke to California and Japan (insert). (b) Tracks of Ioke (blue) and Ioke-generated SPDF *P*-wave sources (red) using the SCSN stations. Locations of *P*-wave sources (*) and storm centers (o) are marked every second day. The insert shows *P*-wave beamformer output on 3 September. (c) Similar to (b), but for the beamformer outputs (September 1–7) from using 79 of the southernmost Hi-net stations.**

Surface waves might be generated in deep water near Ioke. A strong localized cyclone that has not yet interacted with the coast should provide a likely scenario for deep-water generation of SPDF surface waves. Deep-water SPDF *P* waves from Ioke were observed in this study, and Bromirski et al. (2005) observed deep-water SPDF microseisms at the ocean bottom. However, and in contrast, deep-water generated surface waves from Ioke were not identified with the land array data, consistent with studies indicating that non-coastal DF surface-wave microseisms are not observed at land stations (Bromirski, 2001; Bromirski and Duennebier, 2002; Gerstoft and Tanimoto, 2007).

Although the source locations of SPDF *P* waves correlate well with the track of Ioke, they do not necessarily coincide with the locations of the storm center. Despite beamforming bias due to Earth structure heterogeneity, the locations of the *P*-wave peak beam (thus the field of wave-wave interactions) tend to trail Ioke, i.e., in the storm's wake (Figures 8b and 1c), as also observed by Haubrich and McCamy (1969). Opposing waves may develop behind a storm when it overrides its waves. For example, the western quadrant of Ioke forces wind waves southward. If the storm is moving northward faster than the ocean gravity waves propagate, southward traveling wind waves could interact with previously generated northward propagating wind waves at locations behind the storm. However, during August 22 – September 4, *P* waves at 0.2 Hz were generated near Ioke even when the storm propagation speed was less than the group speed of the deep-water ocean waves at 0.1 Hz, i.e., ~ 8 m/s [$c_{group} = g/(4\pi f)$]. This suggests that there must be some wave-wave interactions due to the inhomogeneity of local wave fields even when the storm is stationary.

Power of the SPDF *P* waves generated by Ioke provides a proxy of the intensity of wave-wave interaction under the storm. We made a correction of the SPDF *P*-wave beam power by considering the distance-dependent geometric spreading for *P* waves in a spherically symmetric Earth (Shearer, 2009). The corrected *P*-wave power is compared with the Ioke propagation speed (estimated from the best-track locations at each 6-h time step) and the maximum wind speed (Figure 9), giving correlation-coefficients of 0.72 and -0.66 respectively. Stronger *P* waves were generated when Ioke propagated faster, suggesting that a faster-moving storm may simply increase the area of wave-wave interactions. The lack of positive correlation between the *P*-wave power and wind speed is consistent with the most intense wave-wave interactions occurring not directly under the storm, but after the waves have propagated some distance where they interact with previously generated waves. However, multiple factors may contribute to the intensity of wave-wave interaction. The magnitude and frequency of ocean waves generated by storms is a function of the wind speed, duration, and fetch, each of which vary. In addition, the estimate of *P*-wave energy generated by the storm can be biased due to scattering and lateral structure dependence of attenuation along the storm track.

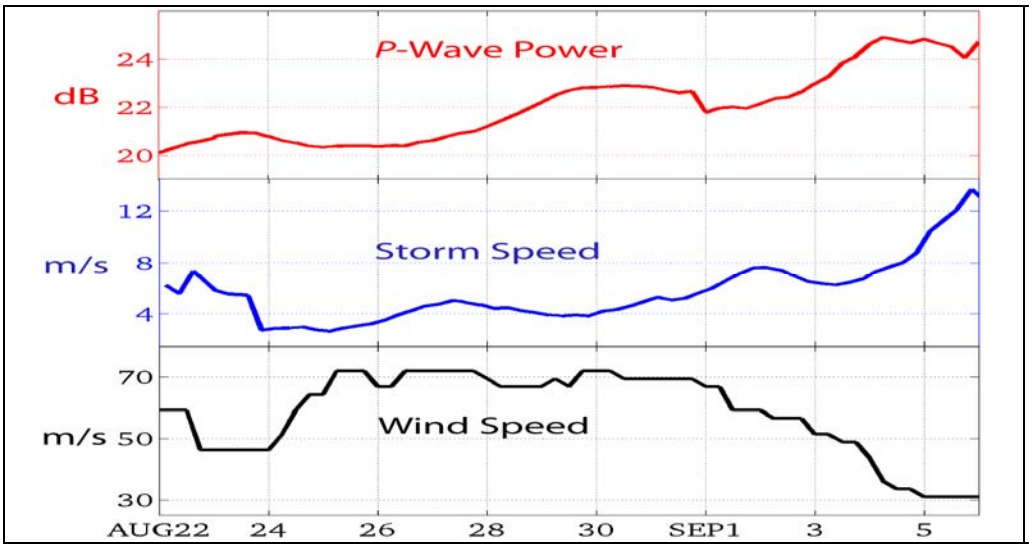


**Figure 9. *P*-wave power (estimated using the peak amplitudes of beamformer outputs and corrected for distance-dependent geometric spreading) compared with storm propagation speed and wind speed.**

Mid-ocean sites exhibit concentrations of DF microseism energy in the SPDF band associated with local wind seas, and in the swell-generated LPDF band linked to near-coastal wave activity (Bromirski et al., 2005). This can be clearly seen in the spectral variation sampled at three F-net stations in Japan (Figures 10a–d) when nearby Ioke transited northwards (September 2–6). Both surface waves and *P* waves likely contribute to the microseism levels observed, although their respective contributions to each band are not known. The different levels of power near 0.2 Hz at the three stations result from their proximity to Ioke and the storm strength at its closest approach to the Japanese coast, with a significant contribution from the storm-associated wave-wave activities at nearby shorelines. Because swell propagates with less dissipation, the differences in the LPDF band between the stations are less. The presence of strong SPDF *P*-wave component in microseisms is also consistent with Tanimoto et al. (2006), who

found that Rayleigh waves appear less dominant above about 0.2 Hz, potentially because of a strong *P* wave contribution.

Swell wave-wave interactions can occur distant from storms, i.e., when incident swell interacts with swell from coastal reflections or from another storm system. This suggests that the Ioke-generated swell may generate *P* waves in the LPDF band distant from the storm. Two relatively distinct *P*-wave source regions are identified for the LPDF and SPDF bands. The beams were calculated and stacked over the 0.10–0.13 Hz, 0.13–0.16 Hz, and 0.18–0.21 Hz when Ioke was weakening. LPDF *P*-wave microseisms tend to be generated closer to the coast (Figure 10e), which is clearly distinct from the deep-ocean SPDF *P*-wave source area near the storm (Figure 10g). Note that the power of the LPDF *P* waves is much less than the SPDF *P* waves. Relatively little *P*-wave energy was generated in the mid-range DF band (Figure 10f), in agreement with the spectral minimum in this band (Figures 10b–d and Bromirski et al. [2005]).

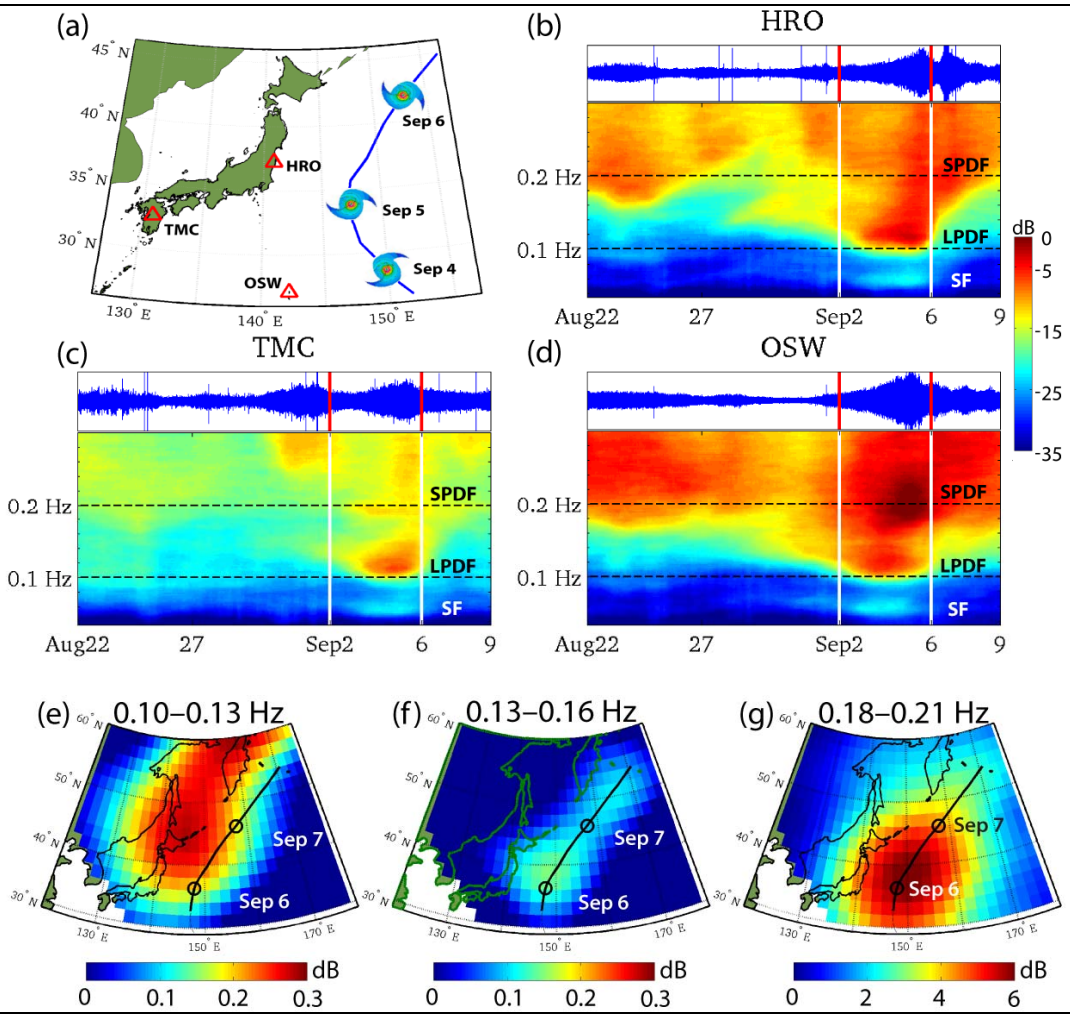


**Figure 10. Spectral partitioning of microseismic *P* waves and their sources. (a) Locations of three individual stations (triangles) and track of Ioke (blue trace). (b–d) Vertical-component time series and spectrograms of the data form HRO, TMC, and OSW. Bands associated with single frequency (SF), long-period double frequency (LPDF), and short-period double frequency (SPDF) microseisms are indicated. Beamformer outputs of *P*-wave sources using the SCSN data are shown for three frequency bands: (e) LPDF, 0.10–0.13 Hz, (f) 0.13–16 Hz, and (g) SPDF, 0.18–0.21 Hz. The beam is averaged over UTC 12-h September 5 through September 7. The trace and circles indicate the temporal locations of the SPDF *P*-wave sources. Note that the beam power is significantly higher in the SPDF band.**

Observations over the whole year 2006 show a seasonal variability of *P*-wave microseism source areas. The dominant SPDF *P*-wave source areas occur in deep oceans (Figure 11a, see also Gerstoft et al., 2008), correlating well with ocean wave height (Tolman, 2005). LPDF *P*-wave microseisms have a stronger coastal component (Figure 11b), generated along Pacific coastlines all year long. In summer, intense wave activity across the South Pacific dominates *P*-wave microseism generation in both bands. In winter, the North Atlantic is also a strong LPDF *P* source region. It is interesting that the Hawaiian Island chain seems to be a hotspot of coastal wave-wave interaction that generates LPDF *P*-wave microseisms in addition to surface waves (Bromirski et al., 2005), as observed for each month in Figure 11b.

For point sources at selected global locations (crosses in Fig. 11 c and 4d), we construct a synthetic beam neglecting amplitude differences, by modeling phase responses corresponding to the travel times at each station, i.e., $\sum_k \exp(i\omega\, \mathbf{t}_{lat[k],lon[k]})$, where $\mathbf{t}_{lat[k],lon[k]}$ describes the travel times from the $k^{th}$ point source to each array stations. Excluding the Hawaiian Island chain, LPDF *P*-wave source areas are modeled for summer and winter months respectively (Fig. 11c and 4d). The simulations do not show significant beamformer leakage near Hawaii, in contrast to the local maximum near Hawaii observed in the real data (Fig. 11b). This suggests that the wave-wave interaction observed near Hawaii is not a processing artifact.

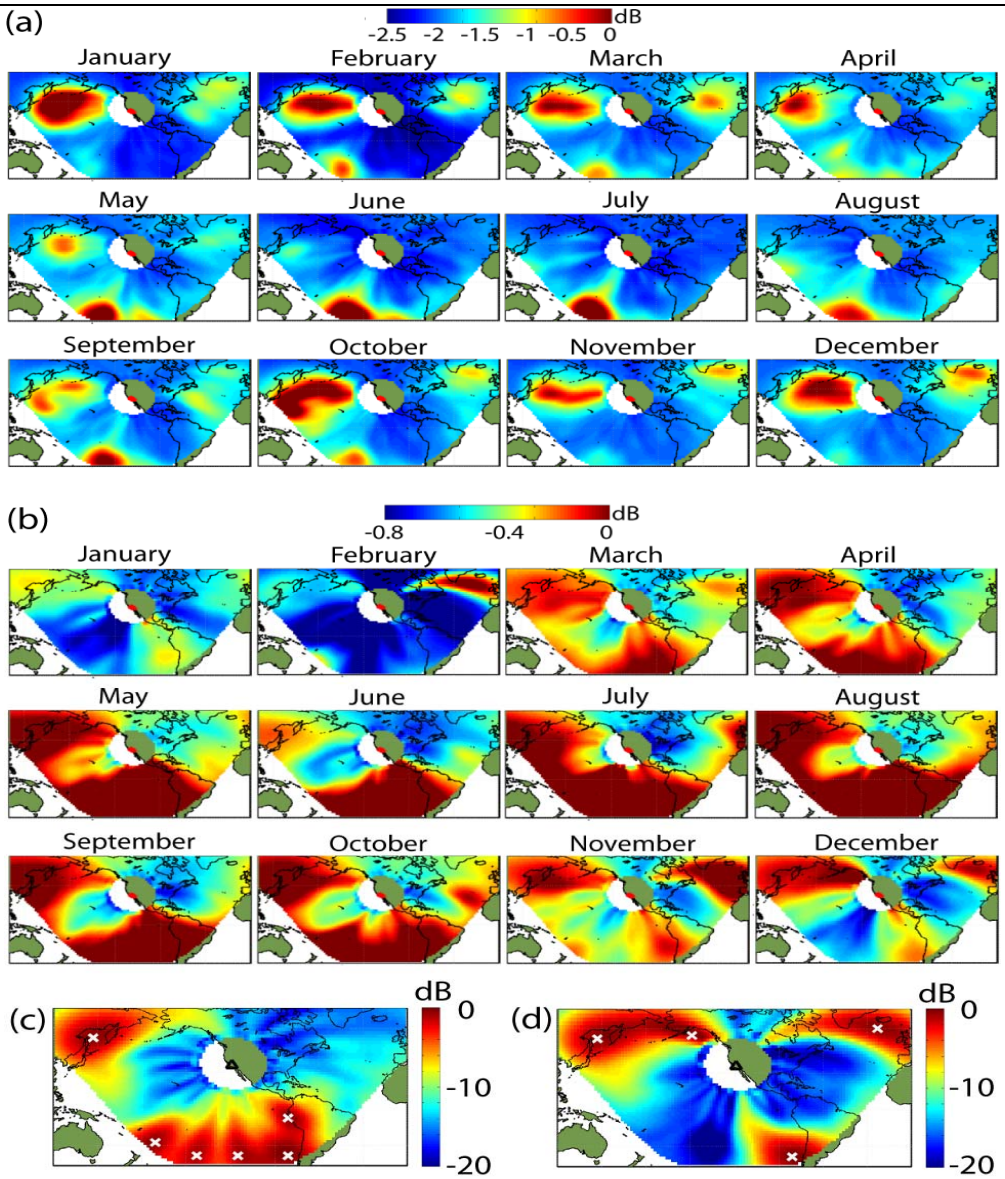


**Figure 11:** ***P*-wave microseism source areas from monthly averaged beamformer outputs using the SCSN data in 2006. (a) SPDF (0.18–0.25 Hz) *P*-wave source areas. (b) LPDF (0.10–0.13 Hz) *P*-wave source areas. The dB scales are independent for SPDF and LPDF bands. (c) Synthetic LPDF *P*-wave beams for summer months, excited by spatially distributed point sources at selected locations (crosses). (d) Synthetics for winter months**.

## CONCLUSIONS AND RECOMMENDATIONS

Using the *P*-wave microseisms of pelagic origin recorded in southern California and generated by Hurricane Katrina, Super Typhoon Ioke, and a South Pacific storm, we have extracted accurate relative *P*-wave arrival times. In practice, a candidate storm is analyzed via array beamforming. Once strong *P* waves are identified and characterized, NCC processing is conducted for obtaining the delay times of *P* arrivals between each pair of stations. Determination of relative arrival times is then realized by solving timing residual equations using least squares. The *P*-wave travel-time anomalies derived from distant storms are similar to those obtained from earthquakes close to the storms. This indicates that oceanic storms may contribute to tomography by providing additional teleseismic sources for imaging Earth structure. Improvements in regional body-wave tomography may come from using oceanic sources that can fill azimuthal gaps in the earthquakes recorded in a particular region.

Beamforming of land-based seismic array data shows clear evidence of deep-ocean origins of SPDF (0.16–0.35 Hz) *P*-wave microseisms due to nonlinear wave-wave interactions of local wind seas near storms. Weaker *P*-wave microseisms are also observable in the LPDF (0.1–0.13 Hz) band, likely associated with swell interactions near the coastlines. These observations show that wave-wave interactions under tropical cyclones may be tracked using land-based seismic arrays. Surface waves generated under the storm were not observed. Further studies with higher density arrays are needed to conclusively determine if surface-wave DF microseisms generated in deep oceans are observed on land.

## ACKNOWLEDGEMENTS

The seismic data were from the Southern California Earthquake Data Center (www.data.scec.org), and the National Research Institute for Earth Science and Disaster Prevention in Japan.

## REFERENCES

Aki, K., A. Christoffersson, and E. S. Husebye (1976). Three-dimensional seismic structure of the lithosphere under Montana LASA, *Bull. Seismol. Soc. Am*. 66: 501–524.

Aki, K., A. Christoffersson and E.S. Husebye (1977). Determination of the 3-dimensional seismic structure of the lithosphere. *J. Geophys. Res.* 82: 277–296.

Bromirski, P. D. (2001). Vibrations from the "Perfect Storm", *Geochem. Geophys. Geosyst.* 2(7), doi:10.1029/2000GC000119.

Bromirski, P. D. and F. K. Duennebier (2002). The near-coastal microseism spectrum: Spatial and temporal wave climate relationships, *J. Geophys. Res*. 107(B8), 2166, doi:10.1029/2001JB000265.

Bromirski, P. D., F. K. Duennebier, and R. A. Stephen (2005). Mid-ocean microseisms, *Geochem. Geophys. Geosyst*. 6, Q04009, doi:10.1029/2004GC000768.

Burg, J. P., and G. C. Burrell (1967). Analysis of K-line wavenumber spectra from the TFO long noise sample, Special Report of *AFTAC Project VT/4053*, *23*.

Cessaro, R. (1994). Sources of primary and secondary microseisms, *Bull. Seismol. Soc. Am.* 84: 142–148.

Chevrot, S., M. Sylvander, S. Benahmed, C. Ponsolles, J. M. Lefevre, and D. Paradis (2007). Source locations of secondary microseisms in western Europe: Evidence for both coastal and pelagic sources, *J. Geophys. Res*. 112: B11301, doi:10.1029/2007JB005059.

Efron, B. (1982). The jackknife, the bootstrap, and other resampling plans. *SIAM*, Philadelphia.

Gerstoft, P., M. C. Fehler, K. G. Sabra (2006a). When Katrina hit California, *Geophys. Res. Lett.* 33: L17308, doi:10.1029/2006GL027270.

Gerstoft, P., K. G. Sabra, P. Roux, W.A. Kuperman, and M. C. Fehler (2006b). Green's functions extraction and surface-wave tomography from microseisms in southern California, *Geophysics* 71: SI23–SI31.

Gerstoft, P., and T. Tanimoto (2007). A year of microseisms in southern California, *Geophys. Res. Lett.* 34: L20304, doi:10.1029/2007GL031091.

Gerstoft, P, P. M. Shearer, N. Harmon, and J. Zhang (2008). Global *P*, *PP*, and *PKP* wave microseisms observed from distant storms, *Geophys. Res. Lett*. 35: L23306, doi:10.1029/2008GL036111.

Guitton, A., and W. W. Symes (2003). Robust inversion of seismic data using the Huber norm, *Geophysics* 68: 1310–1319.

Haubrich, R. A., and K. McCamy (1969). Microseisms: Costal and pelagic sources, *Rev. Geophys.* 7: 539–571.

Humphreys, E. D., and R. W. Clayton (1990). Tomographic image of the southern California mantle. *J. Geophys. Res*. 95: 19, 725–19 746.

Husebye, E. S., A. Christoffersson, K. Aki, and C. Powell (1976). Preliminary results of the 3-dimensional seismic structure of the lithosphere under the USGS Central California Seismic Array. *Geophys. J. Roy. Astron. Soc.* 46: 319–340.

Kang, T. S. and J. S. Shin (2006). Surface-wave tomography from ambient seismic noise of accelerograph networks in southern Korea, *Geophys. Res. Lett.* 33: L17303.

Kedar, S., M. Longuet-Higgins, F. Webb, N. Graham, R. Clayton, and C. Jones (2008). The origin of deep ocean microseisms in the North Atlantic Ocean, *Proc. R. Soc., Ser. A.*, 464: 777–793, doi:10.1098/rspa.2007.0277.

Kennett, B. L. N., E. R. Engdahl, and R. Buland (1995). Constraints on seismic velocities in the Earth from travel times, *Geophys. J. Int.* 122: 108–124.

Koper, K. and B. de Foy (2008). Seasonal anisotropy of short-period seismic noise recorded in south Asia, *Bull. Seismol. Soc. Am.* 98: 3033–3045.

Koper, K., B. de Foy, and H. M. Benz (2010). Composition and variation of noise recorded at the Yellowknife seismic array, 1991-2007, *J. Geophys. Res*., doi:10.1029/2008JB006307.

Lacoss, R. T., E. J. Kelly, and N. M. Toksoz (1969). Estimation of seismic noise structure using arrays, *Geophysics* 34: 21–38.

Landes, M., F. Hubans, N. M. Shapiro, A. Paul, and M. Campillo (2010). Origin of deep ocean microseisms by using teleseismic body waves, *J. Geophys. Res*., doi:10.1029/2009JB006918.

Liang, C., C. A. Langston (2008). Ambient seismic noise tomography and structure of east North America. *J. Geophys. Res.* 113: (B3), B03309, doi:10.1029/2007JB005350.

Lin, F.-C., M. H. Ritzwoller, J. Townend, S. Bannister, and M. K. Savage (2007). Ambient noise Rayleigh wave tomography of New Zealand, *Geophys. J. Int.* 170(2), 649–666.

Lin, F.-C., M. P. Moschetti, and M. H. Rizwoller (2008). Surface wave tomography of the western United States from ambient seismic noise: Rayleigh and Love wave phase velocity maps, *Geophys. J. Int.* 173(1), 281–298.

Longuet-Higgins, M. S. (1950). A theory of origin of microseisms, *Philos. Trans. R. Soc. London, Ser. A.*, 243: 1–35.

Moschetti, M. P., M. H. Rizwoller, and N. M. Shapiro (2007). Surface wave tomography of western United States from ambient seismic noise: Rayleigh wave group velocity maps, *Geochem. Geophys. Geosys*. 8, Q080101, doi:10.1029/2007GC001655.

Paige, C. C., and M. A. Saunders (1982). LSQR: Sparse linear equations and least squares problems. ACM Transactions on Mathematical Software 8/2, 195–209.

Polet, J. (2007). A map of relative *P* wave delay times across southern California, *Geochem. Geophys. Geosys*. 8, Q10003, doi:10.1029/2007GC001626.

Sabra, K. G., P. Gerstoft, P. Roux, W. A. Kuperman, and M. C. Fehler (2005a). Extracting time-domain Greens function estimates from ambient seismic noise, *Geophys. Res. Lett.* 32: L03310, doi:10.1029/2004GL021862.

Sabra, K. G., P. Gerstoft, P. Roux, W. A. Kuperman, and M. C. Fehler (2005b). Surface wave tomography from microseisms in southern California, *Geophys. Res. Lett.* 32: L14311, doi:10.1029/2005GL023155.

Shapiro, N. M., and M. Campillo (2004). Emergence of broadband Rayleigh waves from correlations of the ambient seismic noise, *Geophys. Res. Lett.* 31, L07614, doi:10.1029/2004GL019491.

Shapiro, N. M., M. Campillo, L. Stehly, and M. H. Ritzwoller (2005). High-resolution surface-wave tomography from ambient seismic noise, *Science* 307: 1615–1617.

Shearer, P. M. (1997). Improving local earthquake locations using the L1 norm and waveform cross correlation: application to the Whittier Narrows, California, after shock sequence, *J. Geophys. Res.* 102: 8269–8283.

Shearer, P. M. (2009). *Introduction to Seismology*, Cambridge University Press, Cambridge, UK.

Snieder, R. (2004). Extracting the Green s function from the correlation of coda waves: A derivation based on stationary phase, *Phys. Rev.* E 69: 046610.

Stehly, L., M. Campillo, N. M. Shapiro (2006). A study of the seismic noise from its long-range correlation properties, *J. Geophys. Res.* 111: B10306, doi:10.1029/2005JB004237.

Sutton, G. H., and N. Barstow (1990). Ocean-bottom ultralow-frequency (ULF) seismo-acoustic ambient noise: 0.002 to 0.4 Hz, *J. Acoust. Soc. Am.* 87: 2005–2012.

Tanimoto, T. (2007). Excitation of microseisms, *Geophys. Res. Lett.* 34: L05308, doi:10.1029/2006GL029046.

Tanimoto, T., S. Ishimaru, and C. Alvizuri (2006). Seasonality in particle motion of microseisms, *Geophys. J. Int.*, 166: 253–256, doi:10/1111/j/1365-246X.2006.02931.x.

Toksoz, N. M., and R. T. Lacoss (1968). Microseisms: Mode structure and sources, *Science* 159: 872–873. doi: 10.1126/science.159.3817.872.

Tolman, H.L. (2005). Manual and wave user system documentation of WAVEWATCH-III, NOAA, Camp Springs, Md. (Available at http://polar.ncep.noaa.gov/)

Tsai, V.C. (2009). On establishing the accuracy of noise tomography travel-time measurements in a realistic medium, *Geophys. J. Int.* 178: (3), 1555–1564.

VanDecar, J. C., and R. S. Crosson (1990). Determination of teleseismic relative phase arrival times using multi-channel cross-correlation and least squares, *Bull. Seismol. Soc. Am.* 80: 150–169.

Waldhauser, F., and W. L. Ellsworth (2000). A double-difference earthquake location algorithm: method and application to the northern Hayward fault, California, *Bull. Seismol. Soc. Am.* 90: 1353–1368.

Wapenaar, K. (2004). Retrieving the elastodynamic Green's function of an arbitrary inhomogeneous medium by cross correlation, *Phys. Rev. Lett.* 93: 254301.

Yang, Y., M. H. Ritzwoller, A. L. Levshin, and N. M. Shapiro (2007). Ambient noise Rayleigh wave tomography across Europe, *Geophys. J. Int.* 168: 259–274.

Yang, Y., A. Li, and M. H. Ritzwoller (2008). Crustal and uppermost mantle structure in southern Africa revealed from ambient noise and teleseismic tomography, *Geophys. J. Int.* 174: 235–248.

Yang, Y., and M. H. Ritzwoller (2008). Characteristics of ambient seismic noise as a source for surface wave tomography, *Geochem. Geophys. Geosyst.* 9, doi:10/1029/2007GC001814.

Yao, H., R. D. van der Hilst, and M. V. de Hoop (2006). Surface-wave array tomography in SE Tibet from ambient seismic noise and two-station analysis: I – Phase velocity maps, *Geophys. J. Int.* 166: 732–744.

Yao, H., C. Beghem, and R.D. van der Hilst (2008). Surface-wave array tomography in SE Tibet from ambient seismic noise and two-station analysis: II – Crustal and upper mantle structure, *Geophys. J. Int.* 173: 205–219.

Yao, H., and R. D. van der Hilst (2009). Analysis of ambient noise energy distribution and phase velocity bias in ambient noise tomography, with application to SE Tibet, *Geophys. J. Int.*, in press.

Zhang, J., P. Gerstoft, and P. M. Shearer (2009). High-frequency *P*-wave seismic noise driven by ocean winds. *Geophys. Res. Lett.* 36, L09302, doi:10.1029/2009GL037761.

Zhang, J., P. Gerstoft, and P. M. Shearer (2010a). Resolving P-wave travel-time anomalies using seismic array observations of oceanic storms, *Earth Planet. Sci. Lett.* 292: 419–427, doi:10.1016/j.epsl.2010.02.014.

Zhang, J., P. Gerstoft, and P. D. Bromirski (2010b). Pelagic and coastal sources of P-wave microseisms: Generation under tropical cyclones, *Geophys. Res. Lett.*, in press.

Zheng, S., X. Sun, X. Song, Y. Yang, and M. H. Ritzwoller (2008). Surface wave tomography of China from ambient seismic noise correlation, *Geochem. Geophys. Geosyst.* 9, Q0502, doi:10.1029/2008GC001981.